Real-time terahertz color scanner for moving objects

Takeshi Yasui,[1,*] Ken-ichi Sawanaka,[1] Atsushi Ihara,[1] Emmanuel Abraham,[2] Mamoru Hashimoto,[1] and Tsutomu Araki[1]

[1] *Graduate School of Engineering Science, Osaka University, 1-3 Machikaneyama, Toyonaka, Osaka 560-8531, Japan*

[2] *Centre de Physique Moléculaire, Optique et Hertzienne, UMR5798, Université Bordeaux I, 351, Cours de la Libération , 33405 Talence, France*

[*] *Corresponding author: t-yasui@me.es.osaka-u.ac.jp*

Abstract: Terahertz time-domain spectroscopic (THz-TDS) imaging is an interesting new tool for nondestructive testing and other applications. However, the current speed of image acquisition is relatively low, making it difficult to use for moving objects. In this paper, we propose a real-time THz-TDS line scanner based on electro-optical time-to-space conversion and line focusing of a THz beam. The proposed system functions as a color scanner in the terahertz spectral region with fast line-scanning and has been successfully used to image objects, which are moved on a translation stage. The achieved THz-TDS imaging rate is 23 200 pixels per second. This proposed THz-TDS line scanner has the potential to become a powerful tool for monitoring moving objects in various real-world applications.

OCIS codes: (110.6795) Terahertz imaging; (120.6200) Spectrometers and spectroscopic instrumentation; (300.6495) Spectroscopy, teraherz

References and links

1. D. E. Bray and D. McBride, *Nondestructive Testing Techniques* (John Wiley & Sons, 1992).
2. J. M. Chalmers and P. R. Griffiths, *Handbook of vibrational spectroscopy* (John Wiley & Sons, 2002).
3. D. Abbott and X.-C. Zhang, "T-ray imaging, sensing, and retection," Proc. IEEE **95**, 1509-1513 (2007).
4. D. M. Mittleman, *Sensing with THz radiation* (Springer, 2003).
5. W. Withayachumnankul, G. M. Png, X. X. Yin, S. Atakaramians, I. Jones, H. Lin, B. S. Y. Ung, J. Balakrishnan, B. W.-H. Ng, B. Ferguson, S. P. Mickan, B.M. Fischer, and D. Abbott, "T-ray sensing and imaging," Proc. IEEE **95**, 1528-1558 (2007).
6. B. B. Hu and M. C. Nuss, "Imaging with terahertz waves," Opt. Lett. **20**, 1716-1718 (1995).
7. D. M. Mittleman, S. Hunsche, L. Boivin, and M. C. Nuss, "T-ray tomography," Opt. Lett. **22**, 904-906 (1997).
8. B. Ferguson, S. Wang, D. Gray, D. Abbott, and X.-C. Zhang, "T-ray computed tomography," Opt. Lett. **27**, 1312-1314 (2002).
9. T. Löffler, T. Bauer, K. Siebert, H. Roskos, A. Fitzgerald, and S. Czasch, "Terahertz dark-field imaging of biomedical tissue," Opt. Express **9**, 616-621 (2001).
10. S. Hunsche, M. Koch, I. Brener, and M. C. Nuss, "THz near-field imaging," Opt. Commun. **150**, 22-26 (1998).
11. K. Kawase, Y. Ogawa, Y. Watanabe, and H. Inoue, "Non-destructive terahertz imaging of illicit drugs using spectral fingerprints," Opt. Express **11**, 2549-2554 (2003).
12. Y. C. Shen, T. Lo, P. F. Taday, B. E. Cole, W. R. Tribe, and M. C. Kemp, "Detection and identification of explosives using terahertz pulsed spectroscopic imaging," Appl. Phys. Lett. **86**, 241116 (2005).
13. X. X. Yin, B. W.-H. Ng, B. M. Fischer, B. Ferguson, and D. Abbott, "Support vector machine applications in Terahertz pulsed signals feature sets," IEEE Sensors J. **7**, 1597 – 1608 (2007).
14. X. X. Yin, K. M. Kong, J. W. Lim, B. W.-H. Ng, B. Ferguson, S. P. Mickan, and D. Abbott, "Enhanced T-ray signal classification using wavelet preprocessing," Med. Bio. Eng. Comp. **45**, 611-616 (2007).
15. K. Fukunaga, Y. Ogawa, S. Hayashi and I. Hosako, "Terahertz spectroscopy for art conservation," IEICE Electron. Express **4**, 258-263 (2007).
16. T. Yasui, E. Saneyoshi, and T. Araki, "Asynchronous optical sampling terahertz time-domain spectroscopy for ultrahigh spectral resolution and rapid data acquisition," Appl. Phys. Lett. **87**, 061101 (2005).

#90646 - $15.00 USD Received 7 Dec 2007; revised 11 Jan 2008; accepted 11 Jan 2008; published 16 Jan 2008

17. T. Yasui, Y. Kabetani, E. Saneyoshi, S. Yokoyama, and T. Araki, "Terahertz frequency comb by multifrequency-heterodyning photoconductive detection for high-accuracy, high-resolution terahertz spectroscopy," Appl. Phys. Lett. **88**, 241104 (2006).
18. A. Bartels, A. Thoma, C. Janke, T. Dekorsy, A. Dreyhaupt, S. Winnerl, and M. Helm, "High-resolution THz spectrometer with kHz scan rates," Opt. Express **14**, 430-437 (2006).
19. Q. Wu, T. D. Hewitt, and X.-C. Zhang, "Two-dimensional electro-optic imaging of THz beams," Appl. Phys. Lett. **69**, 1026-1028 (1996).
20. Z. Jiang and X.-C. Zhang, "Electro-optic measurement of THz field pulses with a chirped optical beam," Appl. Phys. Lett. **72**, 1945-1947 (1998).
21. B. Ferguson, S. Wang, D. Gray, D. Abbott, and X.-C. Zhang, "Identification of biological tissue using chirped probe THz imaging," Microelectronics J. **33**, 1043-1051 (2002).
22. Z. Jiang, F. G. Sun, and X.-C. Zhang, "Terahertz pulse measurement with an optical streak camera," Opt. Lett. **24**, 1245-1247 (1999).
23. J. Shan, A. S. Weling, E. Knoesel, L. Bartels, M. Bonn, A. Nahata, G. A. Reider, and T. F. Heinz, "Single-shot measurement of terahertz electromagnetic pulses by use of electro-optic sampling," Opt. Lett. **25**, 426-428 (2000).
24. K. Y. Kim, B. Yellampalle, A. J. Taylor, G. Rodriguez, and J. H. Glownia, "Single-shot terahertz pulse characterization via two-dimensional electro-optic imaging with dual echelons," Opt. Lett. **32**, 1968-1970 (2007).
25. F. G. Sun, Z. Jiang, and X.-C. Zhang, "Analysis of terahertz pulse measurement with a chirped probe beam," Appl. Phys. Lett. **73**, 2233-2235 (1998).
26. T. Yasuda, T. Yasui, T. Araki, and E. Abraham, "Real-time two-dimensional terahertz tomography of moving objects," Opt. Commun. **267**, 128–136 (2006).
27. G. Gallot, J. Zhang, R. W. McGowan, T.-I. Jeon, and D. Grischkowsky, "Measurements of the THz absorption and dispersion of ZnTe and their relevance to the electro-optic detection of THz radiation," Appl. Phys. Lett. **74**, 3450-3452 (1998).
28. Z. Jiang, F. G. Sun, Q. Chen, and X.-C. Zhang, "Electro-optic sampling near zero optical transmission point," Appl. Phys. Lett. **74**, 1191-1193 (1999).
29. F. Miyamaru, T. Yonera, M. Tani, and M. Hangyo, "Terahertz two-dimensional electrooptic sampling using high speed complementary metal-oxide semiconductor camera," Jpn. J. Appl. Phys. **43**, L489–L491 (2004).
30. A. Dobroiu, M. Yamashita, Y. Ohshima, Y. Morita, C. Otani, and K. Kawase, "Terahertz imaging system based on a backward-wave oscillator," Appl. Opt. **43**, 5637–5646 (2004).
31. F. Miyamaru and M. Hangyo, "Finite size effect of transmission property for metal hole arrays in subterahertz region," Appl. Phys. Lett. **84**, 2742-2746 (2004).
32. F. Miyamaru, S. Hayashi, C. Otani, K. Kawase, Y. Ogawa, H. Yoshida, and E. Kato, "Terahertz surface-wave resonant sensor with a metal hole array," Opt. Lett. **31**, 1118-1120 (2006).
33. F. Miyamaru, M. W. Takeda, T. Suzuki, and C. Otani, "Highly sensitive surface plasmon terahertz imaging with planar plasmonic crystals," Opt. Express **15**, 14804-14809 (2007).
34. Y. Watanabe, K. Kawase, T. Ikari, H. Ito, Y. Ishikawa, and H. Minamide, "Component spatial pattern analysis of chemicals using terahertz spectroscopic imaging," Appl. Phys. Lett. **83**, 800-802 (2003).

1. Introduction

In the fields of nondestructive testing, security screening, and biomedical applications, it is important not only to visualize the geometrical shapes of internal structures but also to analyze and identify the chemical composition of test objects. Although both X-rays [1] and ultrasonic waves [1] have been utilized in those applications, the hazardous ionizing effects of the former and the need for direct physical contact in the latter limit their utility. Furthermore, those imaging modalities only produce "monochrome" pictures of a sample, making it difficult to identify its chemical components. Infrared spectroscopy is also frequently used to characterize semiconductors, medicines, and other materials on the basis of the rich spectral fingerprints of molecular vibrational modes in the infrared region [2]. However, infrared scattering severely limits the penetration depth in many samples. In the past decade, terahertz (THz) radiation, lying at the boundary between optical and electrical waves [3], has emerged as a new mode for sensing and imaging [4]. Pulsed THz waves have attractive features such as good penetration for dry, non-polar materials, low scattering, long free-space propagation in dry air, low photon energy, good beam coherence, and broad spectral bandwidth [5]. Since many materials indicate spectral fingerprints in the THz region, the spectroscopic analysis in

#90646 - $15.00 USD Received 7 Dec 2007; revised 11 Jan 2008; accepted 11 Jan 2008; published 16 Jan 2008

this region has received interests as a new tool for material characterizations. Furthermore, the availability of coherent optical imaging has made THz imaging an attractive non-contact, non-ionizing method for a variety of applications. Since the first demonstration of THz transmission imaging in 1995 [6], several other kinds of THz imaging techniques have been reported: reflection tomography [7], computed tomography [8], dark-field imaging [9], near-field imaging [10], and spectroscopic imaging. The last technique in particular permits identification and spatial imaging of the chemical components in a sample on the basis of the THz spectral fingerprints because this imaging modality effectively provides "color" pictures in the THz range in contrast to "monochrome" X-ray and ultrasound imaging. Furthermore, it is straightforward to combine THz spectroscopic imaging with other imaging techniques. Consequently, it has important applications in screening of illicit drugs [11] and explosives [12], detection of cancerous tissue [9] and RNA [13], classification of powders [14], and art conservation [15]. Despite the advantages listed above, however, the technique of THz spectroscopic imaging is hampered by the slow speed of image acquisition.

In a typical THz time-domain spectroscopy (THz-TDS) system, a mechanical translation stage driven by a stepping motor is used for time-delay scanning between the THz pulse and the optical probe pulse. When this system is extended to THz-TDS imaging by raster-scanning the sample through the THz beam focus, the overall image rate can be quite low. As a result, the method has so far only been applied to stationary objects. If THz-TDS imaging can be extended to moving objects in real time, such as industrial products on a conveyor belt, the applications of THz-TDS imaging will be greatly increased. For more rapid sweeps across a range of time delays, a galvanometric scanner or piezoelectric device can be used instead of a stepping motor. However, there is an inherent trade-off between scan range and rate, and thus between spectral resolution and measurement time in THz-TDS. A better alternative would be to eliminate the need for time-delay scanning altogether, which would largely solve the problem of the low imaging rate. Recently, new THz-TDS systems based on asynchronous-optical-sampling [16] or multi-frequency-heterodyning [17] photoconductive detection have been proposed to simultaneously achieve rapid data acquisition and high spectral resolution. In these methods, two asynchronous mode-locked lasers are used for the pump and probe lasers, and thus no mechanical translation stages for time delay scanning are required, thereby overcoming the tradeoff between spectral resolution and measurement time in THz-TDS. Kilohertz rates of time delay have been attained using lasers with a 1-GHz repetition rate and free-space electro-optic sampling (FSEOS) [18]. Unfortunately, many scans have to be integrated together to achieve an adequate signal-to-noise ratio (SNR). Furthermore, mechanical rastering of the sample position is still required.

In many applications, an object is typically moved unidirectionally at a constant speed by a translation stage. To construct a two-dimensional (2D) THz-TDS image of such an object, it would be necessary to acquire and piece together consecutive one-dimensional (1D) THz-TDS images. Real-time acquisition of 1D-THz-TDS images can be achieved if instead of a mechanical stage we use alternative techniques for measuring the time delay and 1D sample position. One effective stage-free configuration combines a single-shot measurement of the temporal waveform with 1D transverse imaging, enabling real-time 2D spatiotemporal (2D-ST) imaging. In the THz region, there have been several reports on single-shot measurements of the temporal waveform of a THz pulse based on 2D-FSEOS [19]. These include time-to-wavelength conversion using a chirped probe pulse [20, 21], use of a THz streak camera [22], time-to-space conversion based on non-collinear 2D-FSEOS [23], and an echelon method [24]. Although some of these techniques could be extended to 2D-ST THz imaging, non-collinear 2D-FSEOS should prove most suitable since it only requires a slight and inexpensive modification of a regular 2D-FSEOS system. More importantly, it has no limitations on time resolution caused by coupling between frequency and time domain methods [25] or by the instrumental response [22]. We have previously proposed a 2D-ST THz imaging technique based on a combination of non-collinear 2D-FSEOS and line focusing of a THz beam onto a sample, and demonstrated the method in a reflection geometry for real-time 2D THz

#90646 - $15.00 USD Received 7 Dec 2007; revised 11 Jan 2008; accepted 11 Jan 2008; published 16 Jan 2008

tomography [26]. Such an imaging technique can also be applied to real-time 1D-THz-TDS imaging in transmission geometry.

In the present paper, we propose to obtain real-time 1D-THz-TDS images of a moving object, which is based on 2D-ST THz imaging by combining non-collinear 2D-FSEOS with line focusing of a THz beam at a sample in the transmission geometry. The proposed system functions as a color-scanner machine in the THz region with fast line-scanning, namely THz-TDS line scanner. After describing the experimental setup and performance, we present some examples of THz-TDS images and movies collected for a moving object.

2. Experimental setup

Figure 1 shows the setup of our THz-TDS line scanner. A femtosecond Ti:sapphire regenerative amplifier (Spectra-Physics Hurricane, pulse energy = 600 μJ, pulse duration = 150 fs, central wavelength = 800 nm, repetition rate = 1 kHz, beam diameter = 10 mm) was employed to generate and detect THz pulses. After diverging the pump light with a plano-concave lens (L1, f = -60 mm), an intense THz pulse is generated via optical rectification of the pump light in a 1-mm-thick, 15-mm-square <110> ZnTe crystal (ZnTe1) manufactured by Nikko Materials of Japan. The THz beam is emitted from the ZnTe1 in collinear with the pump beam, and its radiation angle is about 10°. The THz beam is then collimated by an off-axis parabolic mirror (OAP-M, f = 119 mm). A white polyethylene plate (IRF, thickness = 3 mm) was used as a filter to block the residual laser light. In order to line focus and image or collimate the THz beam, we used three THz lenses (CL1, L2, and CL2) manufactured by Pax of Japan. Figure 1 shows a top view and a side view of the THz beam optics. The first THz cylindrical lens (CL1, f = 50 mm) focuses the THz beam onto the sample, resulting in a line of illumination along the X-axis of the sample. The height of the THz focal line is 20 mm and its width depends on the THz frequency, as discussed later. While passing through the sample, the THz pulse experiences attenuation, delay, and/or distortion due to the frequency-dependent absorption and refractive index. The THz beam is then incident on a 1-mm-thick, 25-mm-square, <110> ZnTe crystal (ZnTe2, manufactured by Nikko Materials of Japan) used for non-collinear 2D-FSEOS, after it has passed through a THz plano-convex lens (L2, f = 100 mm) and a second THz cylindrical lens (CL2, f = 100 mm). As a result of these optics, the THz beam incident on ZnTe2 is collimated in the top view and imaged in the side view (see the imaging ray indicated by the green broken line). Meanwhile, a probe beam is expanded to about 30-mm diameter by a beam expander (BE), and is then polarized linearly by a Glan-laser polarizing prism (P, extinction ratio = 5×10^{-6}, clear aperture = 20 mm diameter). A mechanical stage is used to calibrate the time scale.

The THz and probe beams are incident on ZnTe2 at a crossed angle θ in air. This results in non-collinear 2D-FSEOS for the time-to-space conversion of the pulsed THz electric field. Because the principles of non-collinear 2D-FSEOS are given in detail elsewhere [23, 26], only a brief description of the method is given here. Consider the THz electric field to be composed of a negative and a positive peak with a relative time delay of $\Delta\tau$ (indicated by the blue solid and broken line segments in the top view in Fig. 1). These two negative and positive wavefronts overlap with the single wavefront of the probe beam (the red solid line segment in Fig. 1) at different horizontal positions inside ZnTe2. In this way, the superposed THz electric field at different times peaks at different spatial positions within the transverse profile of the probe beam. This results in a time-to-space conversion factor determined by [23]

$$\Delta\tau = (\Delta h \times \tan\theta) / c, \quad (1)$$

where Δh is the spatial displacement corresponding to the time delay $\Delta\tau$ and c is the speed of light in vacuum. This temporal profile develops successively along the width of ZnTe2. The resulting time window (t_W) and step increment (Δt) are defined as

$$t_W = (D \times \tan\theta) / c, \quad (2)$$

and

#90646 - $15.00 USD Received 7 Dec 2007; revised 11 Jan 2008; accepted 11 Jan 2008; published 16 Jan 2008

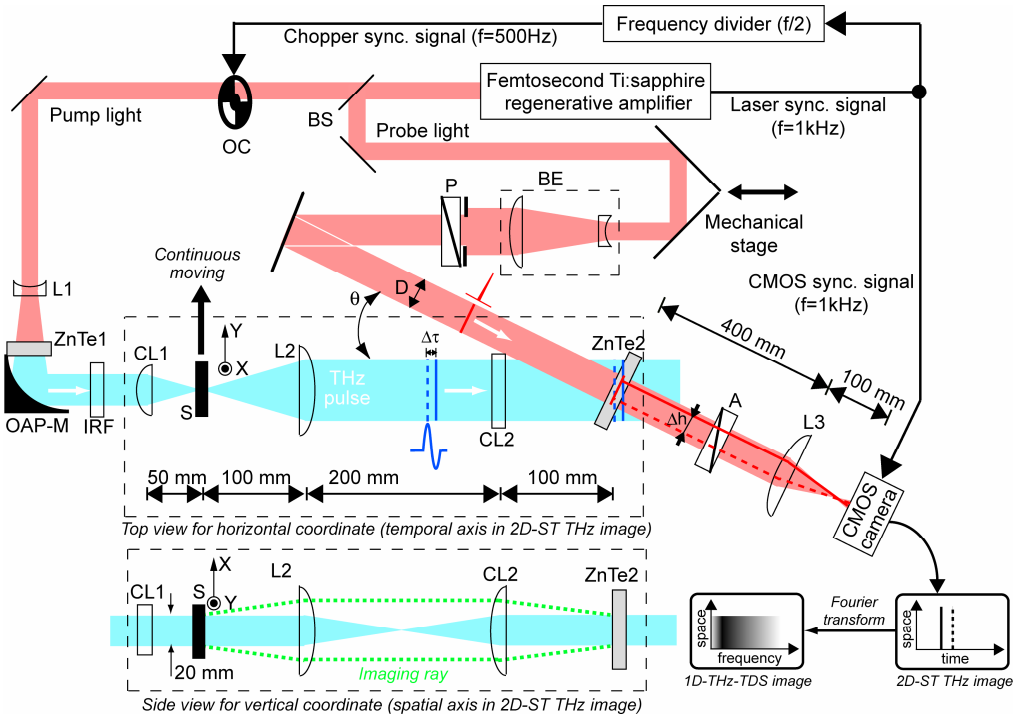

Fig. 1. Experimental setup. BS: beam splitter; OC: optical chopper; L1: plano-concave lens; ZnTe1 and ZnTe2: zinc telluride crystals; OAP-M: off-axis parabolic mirror; IRF: infrared cutoff filter; CL1 and CL2: THz cylindrical lenses; S: sample; L2: THz plano-convex lens; BE: beam expander; P: polarizer; A: analyzer; L3: plano-convex lens.

$$\Delta t = t_W / N = (D \times \tan\theta) / (cN), \tag{3}$$

where D is the diameter of the probe beam and N is the number of pixels across the horizontal coordinate of the 2D imaging device, which is described later. The corresponding frequency resolution ($\Delta\nu$) and range (ν_R) in THz-TDS are

$$\Delta\nu = 1 / t_W = c / (D \times \tan\theta), \tag{4}$$

and

$$\nu_R = \Delta\nu\,(N/2) = (cN) / (2D \times \tan\theta), \tag{5}$$

Therefore, the frequency resolution can be set by proper selection of D and θ. The resolution is improved by increasing D and/or θ. The D value of the setup in Fig. 1 is limited by the clear aperture of P (namely its 20 mm diameter). Furthermore, if the surface of ZnTe2 is perpendicular to the THz beam (as in conventional configurations for non-collinear 2D-FSEOS [23, 26]), the tilted clear aperture of ZnTe2 in the probe beam will limit the D value in the horizontal direction. Therefore, in the setup in Fig. 1, the surface of ZnTe2 is normal to the probe beam. (We confirmed in advance that the differences in the FSEOS efficiencies and distortions of the THz temporal waveform for the two configurations are negligible.) On the other hand, increase of the θ value reduces reflection of the p-polarized THz beam at the front surface of ZnTe2, resulting in increase of THz signal. Given the refractive index of ZnTe (approx. 3.2 below 2 THz [27]) and of air (namely 1), the Brewster's angle at the crystal surface is determined to be 73°. In the present setup where θ = 27°, D = 20 mm, and N = 232 pixels, the values of t_w, Δt, $\Delta\nu$, and ν_R are 34 ps, 0.15 ps, 29 GHz, and 3.3 THz, respectively.

#90646 - $15.00 USD Received 7 Dec 2007; revised 11 Jan 2008; accepted 11 Jan 2008; published 16 Jan 2008

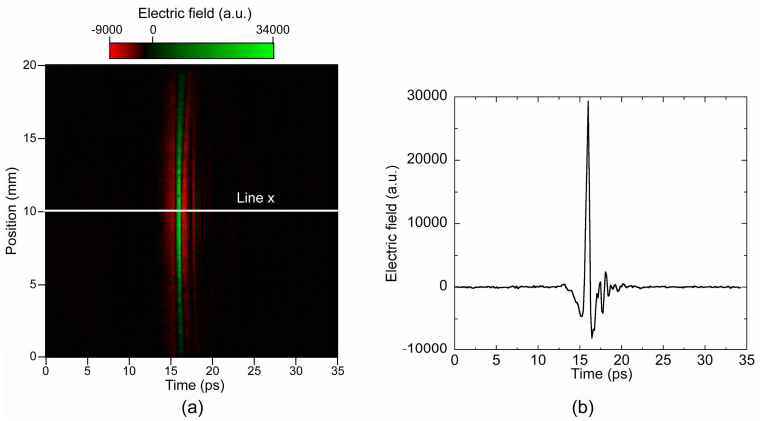

Fig. 2. Time characteristics in the absence of a sample (with a measurement time of 100 ms). (a) 2D-ST THz image and (b) temporal waveform of the pulsed THz electric field along line x in panel (a).

On the other hand, the vertical direction of ZnTe2 is used for 1D transverse imaging of the sample along the THz focal line parallel to the X-axis. In this way, a 2D spatiotemporal (2D-ST) THz image is formed in ZnTe2, in which the temporal profile of the THz pulse and the sample's 1D transverse image develop along the horizontal and vertical dimensions, respectively. The procedure to align the ZnTe2 crystal is as follows. First, the crystal surface is set to be perpendicular to the probe beam at an intersection of the THz beam and probe beam. And then, the crystal position is adjusted along the propagating direction of the probe beam to maximize the THz signal while monitoring the 2D-ST image at real time, resulting in attainment of long interaction length between the THz beam and probe beam in the crystal.

To convert that 2D-ST THz image into a 2D spatial distribution of the probe intensity, FSEOS is performed near the zero optical transmission point [28] using a polarizer P and another, crossed, Glan-laser polarizing prism (A, extinction ratio = 5×10^{-6}, clear aperture = 20 mm diameter). The 2D image of the probe beam is imaged with a demagnification of 0.25 by a lens (L3, f = 80 mm) to a high speed complementary metal-oxide semiconductor (CMOS) camera [Hamamatsu Photonics Intelligent Vision System, sensor area = 4.6 mm × 4.6 mm, pixel size = 232 × 232 pixels, frame rate = 1000 frames per second (fps), exposure time = 1 μs, digital output = 12 bit]. To improve the signal-to-noise ratio (SNR), we adopted a dynamic subtraction technique by synchronizing the camera to the 1 kHz laser pulses [29]. To this end, the pump beam is chopped using an optical chopper (OC) to block every other laser pulse. We perform alternate acquisition of probe images with and without the presence of the THz beam, and then subtract successive images, thereby suppressing the background noise. Finally, a 1D-THz-TDS image of the THz amplitude of the sample along the focal line is obtained by a fast Fourier transform (FFT) of the time dimension in the 2D-ST THz image.

3. Basic performance

3.1 Temporal and spectral characteristics

Figure 2(a) shows a 2D-ST THz image in the absence of a sample after integrating 50 images (corresponding measurement time = 100 ms). The green and red areas in the image indicate positive and negative electric field, respectively. The time scale was calibrated using a known time delay produced by a mechanical stage. The pulsed THz radiation is visible around 16 ps. The fade-out profile of THz signal along vertical direction is mainly due to Gaussian spatial distribution of THz electric field across the beam section. Figure 2 (b) shows a temporal waveform of the THz electric field extracted along the white line *x* in the 2D-ST THz image. The central peak corresponds to a 0.38-ps pulse duration.

#90646 - $15.00 USD Received 7 Dec 2007; revised 11 Jan 2008; accepted 11 Jan 2008; published 16 Jan 2008

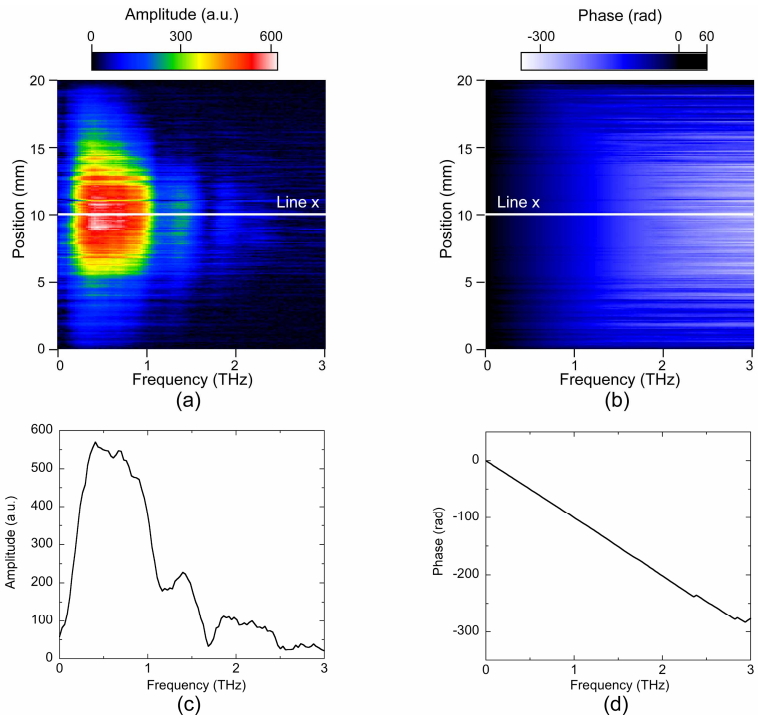

Fig. 3. Spectral characteristics in the absence of a sample (with a measurement time of 100 ms). 1D-THz-TDS images of (a) the amplitude and (b) the phase. Line scans along x of (c) the amplitude and (d) the phase.

An FFT of the time dimension in the 2D-ST THz image results in 1D-THz-TDS images of the amplitude and phase shown in Figs. 3(a) and (b), respectively, for which the frequency resolution is 29 GHz. Figures 3(c) and (d) show respectively the amplitude and phase spectra of the THz radiation extracted along line *x*. Note that the tail of the THz spectra almost reaches 3 THz.

In conventional real-time 2D THz imaging using a CCD or CMOS camera, the small modulations in the probe light induced by the THz electric field are detected despite significant leakage of probe light due to intrinsic birefringence and/or multiple scattering in the ZnTe2 crystal. For detection of a weak signal within the strong background light, a lock-in detection scheme is used. Miyamaru *et al.* have proposed a fast lock-in imaging technique using dynamic subtraction by synchronizing a high-speed CMOS camera to the 1 kHz laser pulses, and have improved the SNR for collinear 2D-FSEOS equipped with a mechanical time-delay stage [29]. On the other hand, for non-collinear 2D-FSEOS, high-speed single-shot measurements of the THz temporal waveform can be achieved because no mechanical time-delay stage is needed. This capability avoids reductions in the SNR due to pulse-to-pulse fluctuations of the amplified femtosecond pulse intensity. To evaluate the effectiveness of combining use of dynamic subtraction detection and single-shot measurements, we investigated the relationship between the SNR and the image integration. Here, the SNR is defined as a ratio of a peak-to-peak value of bipolar, pulsed signal in the presence of THz beam to a standard deviation of noise signal in the absence of THz beam with respect to the temporal waveform of THz electric field. Figure 4 shows the result. Even with no image integration (measurement time = 2 ms, frame rate = 500 fps), a SNR of about 70 was achieved. A power law relationship between measurement time and SNR was found in the form $Y = \alpha X^{\beta}$, where Y is the SNR, X is the measurement time, $\alpha = 47.7$ and $\beta = 0.469$ with a regression coefficient of 0.999. When the system noise is limited by shot noise, the SNR is expected to

#90646 - $15.00 USD Received 7 Dec 2007; revised 11 Jan 2008; accepted 11 Jan 2008; published 16 Jan 2008

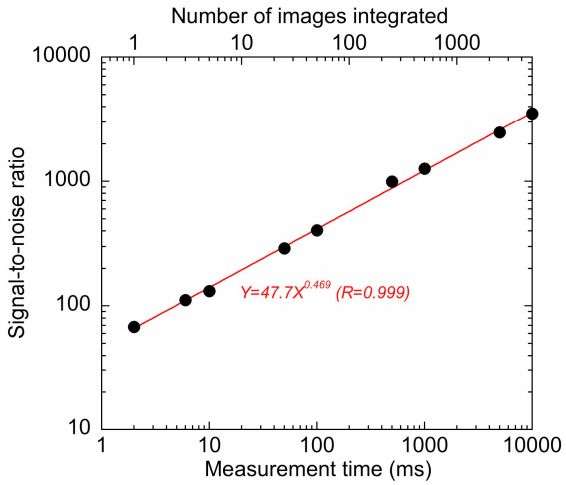

Fig. 4. Relationship between signal-to-noise ratio and measurement time or number of images integrated. The red solid line is a fit to the data in the form $Y = \alpha X^{\beta}$.

be proportional to the square root of the number of images integrated ($Y \propto X^{0.5}$). Therefore, the noise level of the present system is close to the shot-noise limit.

3.2 Imaging characteristics

When investigating the imaging performance of the system, we have to consider the transverse resolution (δ_{line}) and depth of focus (DOF_{line}) of the line focusing lens CL1 with a horizontal numerical aperture (NA) of 0.20, as well as those (δ_{image} and DOF_{image}) of the imaging lenses L2 and CL2 with a vertical NA of 0.22 (see Fig. 1). Assuming that the intensity profile of the THz beam is Gaussian, the theoretical diameter of the focal spot at half-maximum (δ) and the depth of focus (DOF) are [30]

$$\delta = \frac{\lambda f}{d_0}\frac{2\ln 2}{\pi} = \frac{cf}{\nu d_0}\frac{2\ln 2}{\pi}, \tag{6}$$

and

$$DOF = \frac{(d_{min})^2}{\lambda}\frac{\pi}{\ln 2} = \frac{\nu (d_{min})^2}{c}\frac{\pi}{\ln 2}, \tag{7}$$

where λ is the wavelength, f is the focal length of the lens, d_0 is the diameter of the collimated beam at half-height, and ν is the frequency. These equations indicate that the values of δ and DOF depend on the THz frequency. Figures 5(a) and (b) plot δ_{line}, δ_{image}, DOF_{line}, and DOF_{image}, respectively, as a function of frequency. The width of the THz focal line onto a sample is determined by δ_{line} whereas the transverse resolution along the X-direction of a sample [vertical axes in Figs. 3(a) and 3(b)] depends on δ_{image}. The DOF_{line} value determines the tolerance to the thickness and axial positioning of the sample. We must also compare the ZnTe2 thickness to the DOF_{image}. The DOF_{image} value in the setup of Fig. 1 is greater than the ZnTe2 thickness of 1 mm within a 2-THz spectral range, so that there is no degradation of the imaging characteristics. Another factor that could degrade the transverse resolution is the spherical and/or chromatic aberrations of L2 and CL2. Furthermore, the tilt of the ZnTe2 surface relative to the THz beam could deteriorate the imaging characteristics. Therefore the actual transverse resolution of the THz-TDS line scanner is a convolution of those effects.

#90646 - $15.00 USD Received 7 Dec 2007; revised 11 Jan 2008; accepted 11 Jan 2008; published 16 Jan 2008

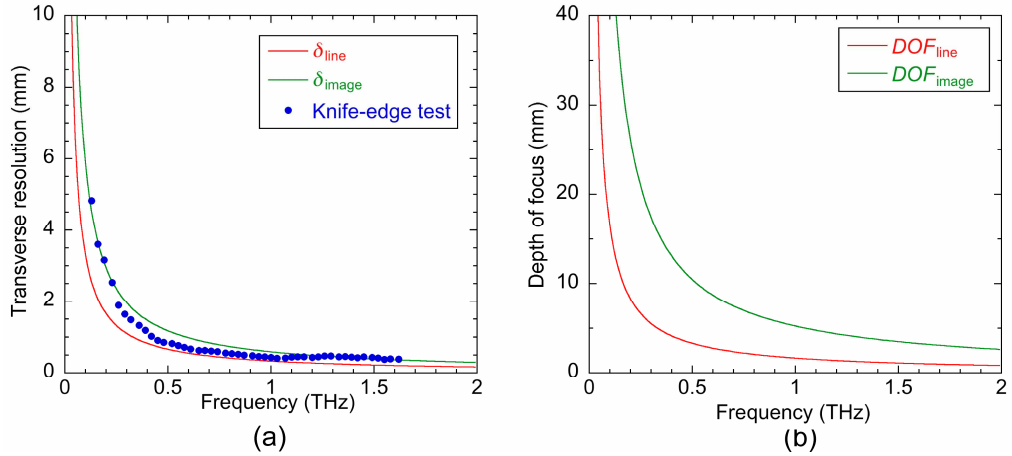

Fig. 5. Theoretical curves of (a) the transverse resolution and (b) the depth of focus for the line focusing and imaging systems of THz beam. δ_{line} and δ_{image} are transverse resolution for the THz line-focusing system (CL1) and the THz imaging system (L2 and CL2) while DOF_{line} and DOF_{image} are depth of focus for the line-focusing system and the imaging system, respectively. The actual transverse resolution, measured by a knife-edge test, is also indicated for comparison.

To measure the actual transverse resolution, we performed a knife-edge test. A 400-μm-thick blade was placed at the sample position to block the upper half of the THz focal line. We measured 2D-ST THz images with and without the presence of the blade, and obtained the corresponding 1D-THz-TDS amplitude images by Fourier transforming the time dimension in the 2D-ST images. To cancel the effect of the uneven amplitude profile along the X-direction, we calculated a ratio of the 1D-THz-TDS image with the blade to that without the blade. Figure 6 (a) shows the resulting ratio image of the THz amplitude as a function of frequency. Figure 6(b) compares knife-edge profiles for various THz frequencies within the spectral range of the present system, which are extracted from amplitude-ratio profiles along vertical image line in Fig. 6(a). Movie of Fig. 6 shows the change in the knife-edge profile as the THz frequency is varied. In this movie, the left panel shows the ratio image of the THz amplitude while the right panel shows the knife-edge profile along the sweeping red line in the ratio image. It can be seen that the slope of the knife-edge profile becomes steeper as the THz frequency increases.

Assuming a Gaussian distribution of THz power across the focal spot, the knife-edge profile can be expressed in terms of an error function (*erf*) as [30]

$$I(x) = I_0 \frac{1}{2}\left[1 + erf\left(2\sqrt{\ln 2}\,\frac{x - x_c}{d}\right)\right], \tag{8}$$

where I_0 is the total intensity of the beam, x is the knife's position, x_c is its position as it crosses the center of the beam, and d is the beam's focused diameter at half-maximum. The square of the knife-edge profile of the THz amplitude ratio equals the corresponding power ratio. We fitted it to Eq. 8 and computed the transverse resolution at each THz frequency. The results are plotted in Fig. 5(a) for comparison with the theoretical values; this figure indicates that the actual transverse resolution attains the diffraction limit of the imaging system. However, the experimental plots are partially better than the theoretical diffraction-limit curve. We consider two reasons for this result. One is an underestimation of THz beam diameter (d_0) in the THz imaging optics. Although we estimated the THz beam diameter from radiation angle of THz beam form ZnTe1 and focal length of OAP-M, the actual beam diameter might be larger than it. In this case, there is a possibility that theoretical diffraction limit is worse than the actual transverse resolution. Other reason is error of the fitting based on Eq. 8 in analysis of the knife-edge test.

#90646 - $15.00 USD Received 7 Dec 2007; revised 11 Jan 2008; accepted 11 Jan 2008; published 16 Jan 2008

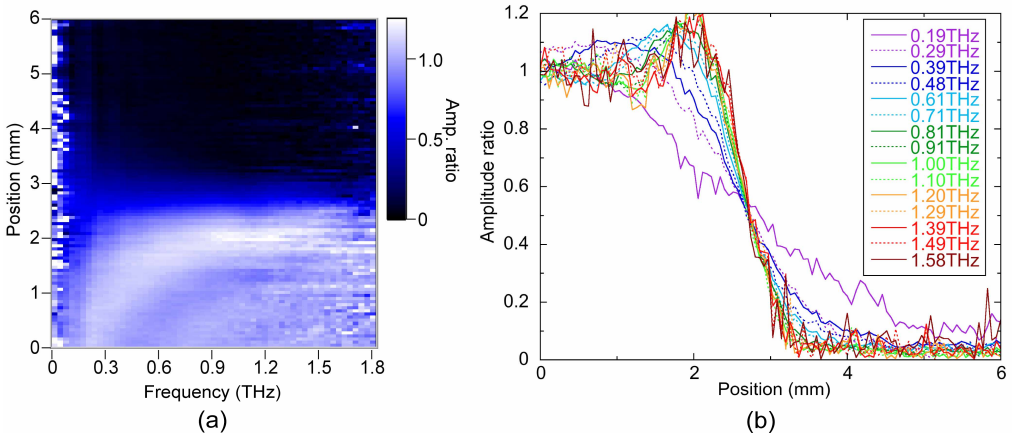

Fig. 6. (3.7 MB) (a) 1D-THz-TDS image of the amplitude ratio around a knife edge. (b) Knife-edge profiles of the THz amplitude ratio at various frequencies.

4. Measurement of a moving object

4.1 Test sample

To test the THz-TDS imaging system, we used as a test sample a metal hole array (MHA) whose spectral characteristics can be designed arbitrarily. It is a metal plate having 2D periodic arrays of circular holes of sub-wavelength diameter. Due to resonant coupling of the incident THz wave with surface plasmon polaritons excited on its surface, the MHA exhibits characteristic optical transmission spectrum at a specific pass-band frequency determined by the hole diameter and spacing. Such MHAs not only serve as band-pass filters with high transmittance in the sub-THz and THz region [31] but can also be used as sensitive THz sensing devices [32, 33]. We used a four-segment MHA (4seg-MHA) made of stainless steel (SUS304) with a thickness of 300 μm manufactured by the Tokyo Process Service Company of Japan. The four segments each have different pass-bands (0.2, 0.4, 0.8, and 1.6 THz) and are distributed spatially as shown in Fig. 7(a). Specifications of the hole sizes and spacings are listed in Table 1.

To characterize the 4seg-MHA, we set up a THz-TDS imaging system to raster scan the MHA sample through the THz beam focus. This system was composed of a Ti:sapphire laser oscillator (Spectra-Physics MaiTai, pulse energy = 12 nJ, pulse duration = 100 fs, central wavelength = 800 nm, repetition rate = 80 MHz), two dipole-shaped low-temperature-grown GaAs photoconductive antennas for THz generation and detection, four off-axis parabolic mirrors (OAP-Ms), a mechanical time-delay stage (with a speed of 22 seconds per scan), and a lock-in amplifier (with a time constant of 10 ms). After being generated at the photoconductive antenna and collimated by the first OAP-M (f = 101.6 mm), the THz beam is focused onto the MHA sample by the second OAP-M (f = 50.8 mm). The diameter of the THz beam focus is calculated to be 4.2 mm at 0.2 THz, 2.1 mm at 0.4 THz, 1.0 mm at 0.8 THz, and 0.52 mm at 1.6 THz, which are the frequencies used for the THz-TDS images described later. The THz beam passing through the sample is re-collimated by the third OAP-M (f = 50.8 mm) and is then focused onto another photoconductive antenna for THz detection using the fourth OAP-M (f = 101.6 mm). For the purpose of THz-TDS imaging measurements, the sample position is raster scanned by a 2D moving stage. The temporal waveform of a 0.35-ps THz pulse was obtained at a SNR of 1100. Also the THz spectrum over a 2 THz range was measured with a resolution of 21 GHz.

#90646 - $15.00 USD Received 7 Dec 2007; revised 11 Jan 2008; accepted 11 Jan 2008; published 16 Jan 2008

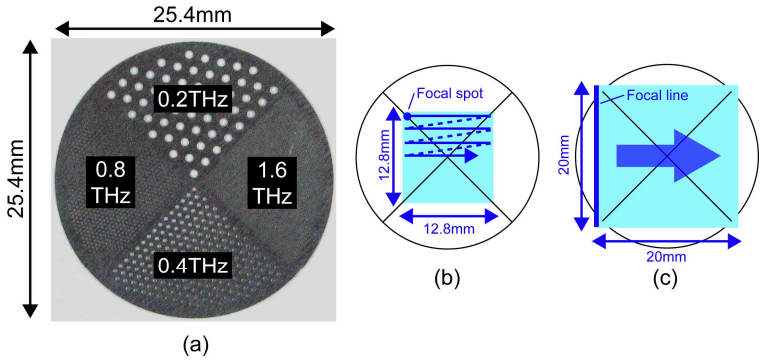

Fig. 7. (a) Photograph of the 4seg-MHA and schematic of the measurement area for (b) the raster-scanning THz-TDS imaging system and (c) the THz-TDS line scanner.

Table 1. Specifications of the four segments of the 4seg-MHA shown in Fig. 7(a).

Pass-band frequency (THz)	Hole diameter (mm)	Hole spacing* (mm)
0.2	0.75	1.5
0.4	0.38	0.75
0.8	0.19	0.38
1.6	0.1	0.19

*Hole spacing is the center-to-center spacing.

The amplitude spectra of THz signal passing through each segment in the 4seg-MHA are shown in Fig. 8. The measured peaks coincide with their specified pass-band frequencies. The substantial peak widths may be caused by dispersion of the incident angle of the focused THz beam onto the sample and/or by an insufficient number of holes within the THz focus spot for resonant coupling with the surface plasmon polaritons. Next we measured THz-TDS images of the 4seg-MHA using the same system. To this end, the sample position was raster scanned within a 12.8 mm × 12.8 mm area using a 2D stage moving at 320 μm/step [see Fig. 7(b)], resulting in a THz-TDS image composed of 41 × 41 pixels. Since the measurement time for the temporal waveform is 22 seconds per pixel, it takes about 10 hours to obtain the image with 41 by 41 pixels. Figure 9 shows the resulting THz-TDS images at 0.189, 0.399, 0.798, and 1.596 THz. Crosstalk between MHA segments in the latter three THz-TDS images is due to the high-frequency tails in the transmission spectra of the MHA areas in Fig. 8. Nevertheless, the image of each MHA area could be easily separated from each other by principal component analysis [34].

4.2 Real-time THz-TDS imaging of a moving object

To test the performance of the proposed method, we measured real-time THz-TDS images of a moving 4seg-MHA. Because the THz beam is line-focused onto the sample, the MHA was continuously moved across it at a rate of 1 mm/s using a translation stage [see Fig. 7(c)]. We collected 500 2D-ST THz images per second for 20 seconds, and integrated each group of 50 images to end up with 200 2D-ST THz images. The acquisition speed of the vertical line image was 10 lines per second. The SNR in this case is estimated from Fig. 4 to be 403 in the absence of a sample. Next, 1D-THz-TDS amplitude images were obtained by Fourier transforming the time dimension in the 2D-ST images. Finally, we obtain successive THz-TDS images at an increment of frequency resolution of 29 GHz by rearranging a set of 200 1D-THz-TDS images with regard to THz frequency. The resulting THz-TDS images and movies of the 4seg-MHA at 0.204, 0.407, 0.815, and 1.600 THz are shown in Fig. 10(a) and its movie with an image size of 20 mm × 20 mm, corresponding to 200 × 232 pixels. Crosstalk between MHA segments is again seen. By comparison with the THz-TDS images

#90646 - $15.00 USD Received 7 Dec 2007; revised 11 Jan 2008; accepted 11 Jan 2008; published 16 Jan 2008

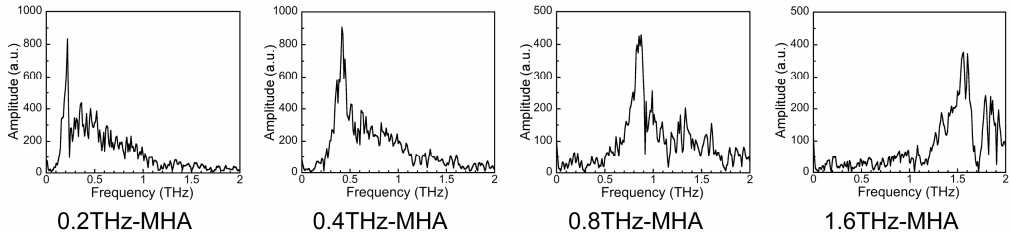

Fig. 8. Transmission spectra of each segment of the 4seg-MHA of Fig. 7(a) measured using a raster-scanning THz-TDS imaging system.

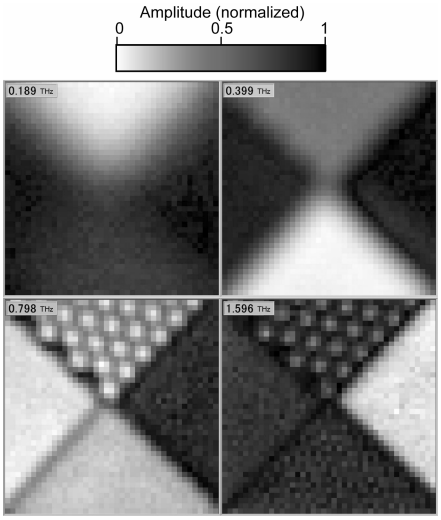

Fig. 9. THz-TDS images of the 4seg-MHA at four THz frequencies measured using a raster-scanning THz-TDS imaging system. Each image consists of 41 by 41 pixels.

obtained by the raster-scanning system (see Fig. 9), we conclude that the proposed THz-TDS line scanner measured the moving 4seg-MHA correctly. It is important to note that this movie is not a fast-forwarding movie but a "real-speed" movie of the measurement. Thus the present system can generate vertical line images of a moving sample consecutively in the order depending on the movement at all THz frequencies. Here, we consider a possibility that integration of 50 2D-ST THz images blurs the THz-TDS images in Fig. 10(a). In this demonstration, 10 000 2D-ST THz images were measured for the sample movement of 20 mm (2 μm/image). Hence, integration of 50 images is corresponding to averaged image for the sample movement of 100 μm. Since the sample movement of 100 μm is smaller than the width of THz focal line within the spectral range of 2 THz [see δ_{line} curve in Fig. 5(a)], one can neglect the reduction of spatial resolution caused by the image integration of the moving object. In this way, the proposed system can be applied for moving object. The fade-out profile of THz signal along vertical direction is due to the Gaussian spatial distribution of THz amplitude across the beam section, which is caused by the beam profile of the pump light. Effect of such profile will be improved by two methods. One is to change the Gaussian beam profile of the pump light to a top-hat profile by use of the beam shaping techniques. Another is use of ratio of the 1D-THz-TDS amplitude image with the 4seg-MHA to that without the 4seg-MHA.

To evaluate the limit on the speed of the sample, we increased the motion of the 4seg-MHA to 10 mm/s. We acquired 1000 2D-ST THz images for 2 seconds at 500 fps and integrated groups of 5 images to maintain a sufficient number of vertical image lines (10 line/mm) in the THz-TDS images. The SNR in this case, with a 100 line/s acquisition speed, is estimated from Fig. 4 to be 132 in the absence of a sample. THz-TDS images acquired in

#90646 - $15.00 USD Received 7 Dec 2007; revised 11 Jan 2008; accepted 11 Jan 2008; published 16 Jan 2008

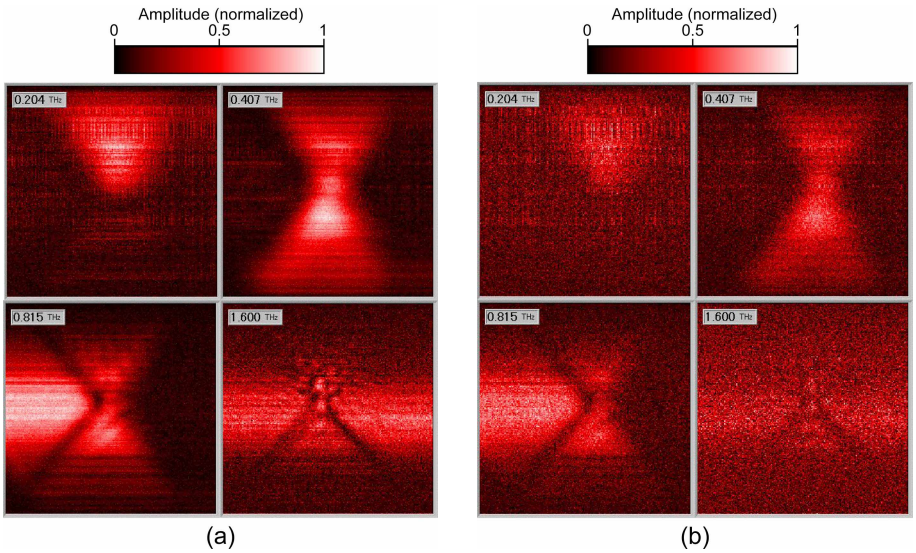

Fig. 10. THz-TDS images of the 4seg-MHA at four frequencies measured by real-time THz-TDS line scanner with the sample moving at (a) (1.5 MB) 1 mm/s and (b) (1.3 MB) 10 mm/s. Each image consists of 200 by 232 pixels.

the aforementioned manner and a movie of the 4seg-MHA at 0.204, 0.407, 0.815, and 1.600 THz are shown in Fig. 10(b) and its movie with an image size of 20 mm × 20 mm, corresponding to 200 × 232 pixels. Even at this sample speed of 10 mm/s, the THz-TDS images at 0.204, 0.407, and 0.815 THz still show the spectral characteristics of the 4seg-MHA, despite the decreased SNR. On the other hand, in the THz-TDS image at 1.600 THz, the signal for the 1.6-THz MHA segment has been quite low. This is mainly due to the decreased SNR and to the limited dynamic range of the signal at higher THz frequencies. Improvement of the SNR and/or increase in the THz spectral bandwidth would permit THz-TDS imaging of fast-moving objects at higher THz frequencies.

Finally, we compare the presented THz-TDS line scanner with the conventional raster-scanning THz-TDS imaging system in regards to image pixel rate. Figure 11 compares successive THz-TDS images obtained by the raster-scanning system and the line scanner. In the raster-scanning system, with a measurement time for the temporal waveform of 22 seconds per pixel, it requires 36 982 sec to acquire an image with 41 by 41 pixels [see Fig. 11(a)]. We here have to consider difference of frequency resolution between the two systems for fair comparison of the pixel rate because measurement time is dependent on frequency resolution in the raster-scanning system. In Fig. 11, frequency resolution of the raster-scanning system (= 21 GHz) was 1.38 times better than that of the line scanner (= 29 GHz). If the frequency resolution of the raster scanning system is set to be 29 GHz, the measurement time of the 4seg-MHA is estimated to be 26 780 sec. The resulting pixel rate is thus only 0.063 pixel/s. For the line scanner with a sample speed of 1 mm/s, an image with 200 by 232 pixels can be obtained in 20 seconds [see Fig. 11(b)]. The resulting pixel rate is as high as 2320 pixel/s, which is 36 825 times higher than that of the raster-scanning system. Furthermore, when the sample speed is increased to 10 mm/s, the line scanner attains a pixel rate of 23 200 pixel/s [see Fig. 11(c)]. On the other hand, the SNR of the raster-scanning system is about 10 times better than that of the line scanner for a sample speed of 10 mm/s because a lock-in amplifier is used in the raster-scanning system. To achieve a SNR similar to that of the raster-scanning system, the line scanner would require a measurement time of 163 s per THz-TDS image (see Fig. 4), corresponding to a rate of 285 pixel/s. We conclude that the line scanner is superior to the raster-scanning system with regard to the pixel rate.

#90646 - $15.00 USD Received 7 Dec 2007; revised 11 Jan 2008; accepted 11 Jan 2008; published 16 Jan 2008

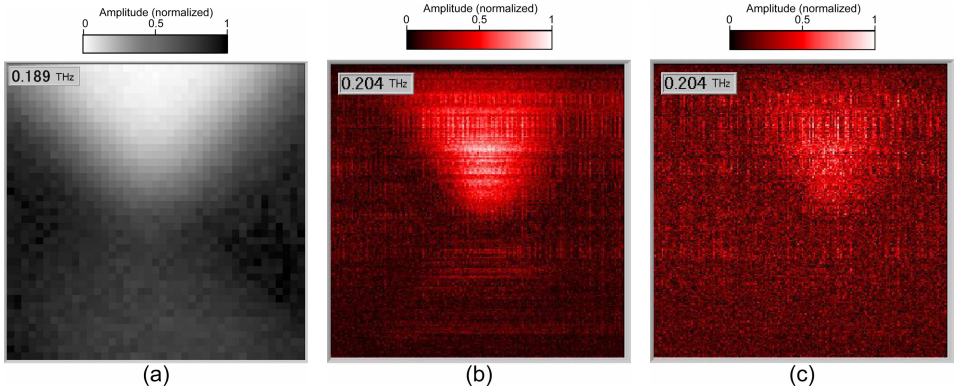

Fig. 11. Successive THz-TDS images of the 4seg-MHA measured by (a) (1.1 MB) raster-scanning THz-TDS imaging system, (b) (1.0 MB) real-time THz-TDS line scanner (sample speed = 1 mm/s), and (c) (1.5 MB) real-time THz-TDS line scanner (sample speed = 10 mm/s).

5. Conclusion

We have developed a real-time THz-TDS line scanner that can be used to image moving objects. The proposed method is based on 2D-ST THz imaging by combining non-collinear 2D-FSEOS with line focusing of a THz beam onto a sample. 2D-ST images with a size of 20 mm by 34 ps were obtained at a high SNR by adopting a 500-Hz lock-in imaging technique as well as image integration. FFT calculation of the time dimension in the 2D-ST THz images gives 1D-THz-TDS images of size 20 mm by 3 THz at a frequency resolution of 29 GHz. The spatial resolution of the proposed THz-TDS scanner depends on the THz frequency but is near the diffraction limit of the imaging optics. We applied the technique to successfully image a moving 4seg-MHA. The pixel rate of the THz-TDS line scanner was as high as 2320 pixel/s and 23 200 pixel/s for sample speeds of 1 mm/s and 10 mm/s, respectively. These are much higher pixel rates than those of a raster-scanning THz-TDS imaging system. To the best of our knowledge, this is the first time that THz-TDS imaging of a moving object has been achieved. Consequently, this method has the potential to become a powerful tool for monitoring moving objects in real-world applications.

Acknowledgements

This work was supported by Grants-in-Aid for Scientific Research Nos. 18686008 and 18650121 from the Ministry of Education, Culture, Sports, Science, and Technology of Japan, the Sumitomo Foundation, and a Sasakawa Scientific Research Grant.

#90646 - $15.00 USD Received 7 Dec 2007; revised 11 Jan 2008; accepted 11 Jan 2008; published 16 Jan 2008